



Degradation study by 3D reconstruction of a nickel–yttria stabilized zirconia cathode after high temperature steam electrolysis operation



E. Lay-Grindler^a, J. Laurencin^{a,*}, J. Villanova^b, P. Cloetens^b, P. Bleuet^c, A. Mansuy^a, J. Mougín^a, G. Delette^a

^a Univ. Grenoble Alpes/CEA, LITEN, F-38054 Grenoble, France

^b ESRF, 6 rue Jules Horowitz BP 220, 38043 Grenoble, France

^c Univ. Grenoble Alpes/CEA, LETI, MINATEC Campus, F-38054 Grenoble, France

HIGHLIGHTS

- Microstructural evolution of Ni–YSZ cermet is analysed after steam electrolysis operation.
- Ni coarsening is quantified by 3D reconstructions.
- Reconstructions are obtained from synchrotron X-ray nano-tomography.
- Impact of Ni agglomeration on cell performances is evaluated through an in-house model.
- The cell voltage degradation due to Ni agglomeration is $\approx 1.3\%/1000$ h.

ARTICLE INFO

Article history:

Received 29 April 2014

Received in revised form

8 July 2014

Accepted 11 July 2014

Available online 19 July 2014

Keywords:

Ni–YSZ

Microstructure

Coarsening

X-ray tomography

SOEC

ABSTRACT

Microstructural evolution of a Solid Oxide Electrolyser Cell (SOEC) Ni–YSZ cermet cathode is investigated using three dimensional electrode characterisations. 3D reconstructions are obtained on a reference and two long-term tested cells, which were maintained at -0.5 and -0.8 A cm⁻² for 1000 h at 800 °C. During the long term tests, air was fed at the anode and a mixture of 10% H₂–90% H₂O was fed at the cathode. In this framework, reconstructions have been obtained from synchrotron X-ray nano-tomography technique. Microstructural properties extracted from the 3D reconstructions exhibit an evolution during the tests. Triple Phase Boundary length is decreasing from 10.49 ± 1.18 μm⁻² for the reference cell to 6.18 ± 0.6 μm⁻² for the long term tested cell at -0.8 A cm⁻². Evolutions of morphological parameters were introduced in an in-house multi-scale model to evaluate their impacts on the electrode degradation, and hence, on the global SOEC performance.

© 2014 Elsevier B.V. All rights reserved.

1. Introduction

High temperature steam electrolysis has a great potential for an efficient production of hydrogen. Indeed, this system produces hydrogen and oxygen from water vapour, with no greenhouse gas emissions. It is particularly attractive in a context of renewable energy for conversion and storage, e.g. when wind or solar energies are available. Nevertheless, the poor durability of this system is one of the main drawbacks of this technology. Indeed, Solid Oxide Electrolyser Cells (SOECs) performance currently decrease by few percent (about 2–5%) after 1000 h of operation [1,2], whereas an

economic viability would be achieved for a degradation limited to few tenth of percent (<0.5%).

These degradations are mainly attributed to material deteriorations occurring in operation, such as electrodes microstructural evolutions or material chemical decomposition. Conversely to Solid Oxide Fuel Cells, few papers in literature have been dedicated to assess the SOEC stability over a long term of operation (>500 h). For e.g., Schefold et al. [1] have reported a 9000 h test carried out at $T = 780$ °C in SOEC galvanostatic conditions. A typical cathode supported cell was used for the experiment which was constituted of Yttria-Stabilised Zirconia (YSZ) for the electrolyte, Lanthanum Strontium-substituted Ferrite/Cobaltite (LSCF) for the anode and a nickel-YSZ cermet (Ni–YSZ) for the cathode. In that conditions, the authors have measured a mean voltage loss of 3.8% per 1000 h.

* Corresponding author. Tel.: +33 (0) 438782210.

E-mail address: jerome.laurencin@cea.fr (J. Laurencin).

Hauch et al. [2] have also reported long-term tests performed at 850 °C on Ni–YSZ cathode supported cells (YSZ for the electrolyte and a composite made of YSZ and Lanthanum Strontium-substituted Manganite (LSM) for the anode). They found an average cell voltage degradation rate of 2%/1000 h for a test of 1316 h. Even if all the mechanisms are not still fully understood, it seems that the main underlying process of degradation is mostly caused by atoms self-diffusion or inter-diffusion between the SOEC constituents. Indeed, at the considered high temperature of operation, those phenomena are rapid, and atoms are able to migrate through the interfaces, penetrate inside the materials, form secondary phases and modify the material functionality. The main degradation phenomena reported in literature are the followings:

- (i) Nickel agglomeration in the cermet [2,3].
- (ii) Oxygen electrode delamination [4–7].
- (iii) Chromium poisoning of the oxygen electrode from the interconnection material [6].
- (iv) Cations segregation, and phases precipitation in the different materials, such as a secondary phase formation between anode and electrolyte [8].
- (v) Contamination (Ni, Cr, Si, Al ...) of active sites [2,7,9]. Note that Cr can be released from the metallic interconnects, Si is liable to come from the glass seal material, while Al can originate from alumina addition for sintering aid during the cell manufacturing process.
- (vi) Ionic conductivity loss of the electrolyte material because of the electro-reduction of the electrolyte [4,10,11].

In this context, it appears essential to quantify the actual morphological evolution of the classical cathode material used for SOEC, a cermet of nickel and yttria-stabilized zirconia (Ni–YSZ). It is worth noting that several 3D reconstructions of this electrode have been already reported in literature [12–21]. Nevertheless, among all these studies, very few have been dedicated to assess the three dimensional cermet microstructure change in operation [14,15,20,21]. For instance, Wilson et al. [14] and Nelson et al. [15] have compared the microstructure of a reference cell and a cell that was tested up to 1130 h in SOFC mode. They observed an

agglomeration of the smallest Ni particles resulting in a significant Ni coarsening. It can be noticed that all the aforementioned articles have been dedicated to a Solid Oxide Fuel Cell (SOFC) purpose but, according to our best knowledge, no study has been yet devoted to the SOEC mode of operation.

In order to determine the extent of the degradation related to the Ni–YSZ electrode in electrolysis mode, microstructural evolution of the cathode functional layer is investigated using a 3D reconstruction technique, both on a reference and on long-term tested cells. In this study, 3D reconstructions have been obtained from synchrotron X-ray nano-holotomography, and then used to calculate/compute the microstructural parameters evolution upon operation. These properties have been introduced in an in-house micro-model [22] to determine their impact on the electrode behaviour. In order to estimate the influence of the microstructure degradation on the global cell polarisation curve, the local approach has been coupled to a home-made SOEC macro-model [23].

2. Experimental part

2.1. Samples

Commercial SOEC cathode supported cells, supplied by HC Starck producer, were used in this study. The materials, structure, and typical dimensions of the cell are illustrated in Fig. 1:

- The cathode consists of a thin ($\approx 10 \mu\text{m}$) functional layer deposited on a thick (500 μm) cathode current collector. A thin layer of pure Ni is deposited on the top of the current collector in order to improve the electrical contact with the metallic interconnect. As received, the functional layer and the current collector are composed of nickel oxide (NiO) and zirconia ZrO_2 stabilized with 8 (8YSZ) and 3 (3YSZ) mol.% of Y_2O_3 , respectively, for the functional and the current collector layers. It can be noticed that 3YSZ is used for the support instead of 8YSZ in order to improve the mechanical robustness of the cell. Indeed, it is reminded that the 3YSZ bending strength is much higher than the characteristic strength of 8YSZ (*i.e.* 1300 MPa for 3YSZ vs 230 MPa for 8YSZ [24]).

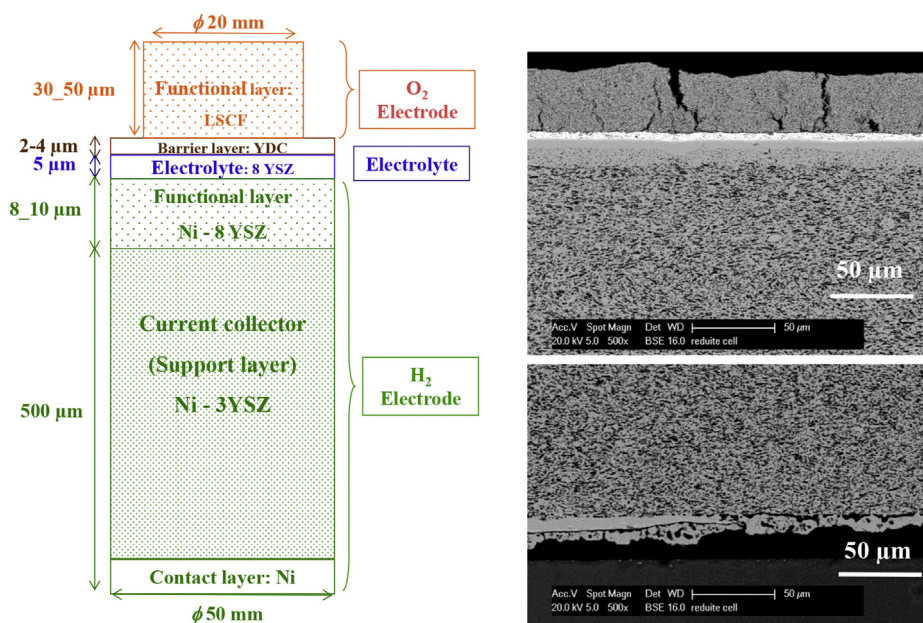


Fig. 1. Schematic representation of the cell structure. The global view of cell layers are illustrated by two polished cross section images obtained with a Scanning Electron Microscope (SEM) in Back Scattering Electron (BSE) mode (for the cell in its reduced state).

- On the top of the cathode functional layer, the following layers are successively deposited: a 5 μm thick and dense 8YSZ electrolyte, a 2–4 μm thick yttria doped ceria (YDC) barrier interlayer and the anode material, which consists of a 30–50 μm thick $\text{La}_{0.6}\text{Sr}_{0.4}\text{Co}_{0.2}\text{Fe}_{0.8}\text{O}_3$ (LSCF) material. Cathode and electrolyte diameter is 50 mm while the diameter of YDC protective layer and LSCF anode is 20 mm.

In its reduced state, the cathode functional layer is composed of 78 wt% of Ni and 22 wt% of 8YSZ. Fig. 2 displays a polished cross of the functional layer examined with a Scanning Electron Microscope (SEM). The mean porosity of the interlayer has been assessed by image analysis on different zones of the 2D micrographs. By this technique, the porosity of the cathode functional layer has been roughly estimated to $\approx 18\%$.

A zoom in the functional layer is also shown in Fig. 2. The micrograph reveals the characteristic sizes of the microstructure. It can be observed that the typical dimension of pores ranges in the order of ≈ 0.7 –1 μm while the characteristic length of the Ni particles is in the order of ≈ 0.8 –1.8 μm .

2.2. Long term tests

Three cells were used in this study. Each of them was heated up to 800 $^{\circ}\text{C}$ with pure hydrogen at the cathode side to reduce the nickel oxide of the cathode. The reference cell was cooled down at -0.5 $^{\circ}\text{C min}^{-1}$, while the other cells were maintained at -0.5 and -0.8 A cm^{-2} for 1000 h at 800 $^{\circ}\text{C}$ before being cooled down in the same conditions than the reference cell. During the long term tests, air was fed at the anode and a mixture of 10% H_2 –90% H_2O was fed at the cathode (12 $\text{mL min}^{-1} \text{cm}^{-2}$ at each electrode) [25].

2.3. Synchrotron X-ray nano-holotomography technique

Microstructures of SOEC cathode functional layers of reference and aged cells were investigated by X-ray nano-holotomography on beamline ID22NI of the European Synchrotron Radiation Facility (ESRF). This third generation of synchrotron provides a hard X-ray beamline with a high level of brilliance. This feature allows inspecting large volume of electrode despite the strong X-ray absorption of the studied materials. Valuable reconstructions are thus obtained with both high spatial resolution and large field of view [12,26].

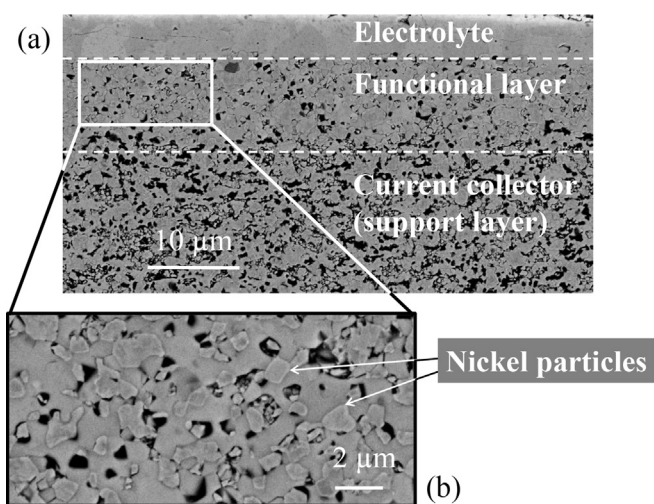


Fig. 2. BSE-SEM image of the polished cell cross section (for the cell in its reduced state): (a) Global view of the cathode functional layer sandwiched between the electrolyte and the cell support, (b) Zoom on a part of the functional layer.

The experimental procedure allows obtaining the raw data of 3D electrodes reconstructions. The procedure has been already described in Refs. [12,26] and is summarised hereafter.

To prevent any cell interfacial degradation during the sample preparation and to enhance the phase separation during tomography, the porous electrodes were firstly embedded in a specific epoxy resin (E505 Epotecny[®]) [26]. Strips (1 or 2 mm large) containing the full stack of layers were then extracted using a wire saw. They were afterwards polished using the computer controlled polishing system Centar (Gatan, Inc) and progressively thinned down to 100 μm . Finally, strips were wire sawed in the perpendicular direction to produce needles of 100 μm cross-section, containing the whole stack of SOEC layers [12]. For mounting on the tomography rotation stage, the sample was placed in a 100 μm -diameter quartz glass capillary. X-ray nano-holotomography was then carried out following the standard procedure of the beamline. Experiments were carried out using an X-ray energy of 29.6 keV. It is worth mentioning that such high energy level is required because of the strong X-ray absorption of the SOEC materials and the necessity to inspect large volume of material [12,26]. The obtained 3D reconstruction presents a volume of $\approx 105,500 \mu\text{m}^3$ with a voxel size of 25 nm [26].

The volume was reconstructed from the projections using standard holotomography techniques, especially by filtering and segmentation steps as described in Ref. [26]. To summarize, each voxel is attributed to an electrode phase: in other words, each peak of the grey levels histogram is associated to one of the electrode phases. This segmentation step is capital, since artefacts could be resulting from the attribution of more voxels to one phase to the detriment of another phase. For this reason, a 3D numerical image processing has been implemented in Matlab[®] [26]. In a first step, images are filtered based on an anisotropic diffusion process. This filter, which was initially proposed by Perona and Malik [27], simultaneously makes uniform the grey levels inside the phases, and increases the contrast at the boundaries. It has been shown that this filtering is especially well adapted to process Ni–YSZ cathodes images since it substantially improves the separation of each peaks of the grey level distribution [26]. In a second step, the 3D reconstruction is segmented according to a numerical approach developed by Otsu [28]. This method is based on a statistical analysis of grey levels distribution, and it is one of the most qualified methods for pores and electrodes materials segmentation [29]. Moreover, the method allows the computing of a criterion that indicates the quality of the segmentation.

After image filtering and segmentation, the obtained 3D reconstructed volumes are used to quantify the electrode microstructure properties. The numerical procedures developed to calculate these properties are described in the next section.

3. Microstructure calculations

Microstructure calculations were executed on the 3D reconstructions by using a set of programs implemented in Matlab[®] software and Cast3M Finite Element solver [30]. The procedures have been fully described in Refs. [12,31]. Only the main steps are recalled in the following:

- (i) Volume fraction of one phase is directly given by the percentage of voxels belonging to the analysed phase [12].
- (ii) The density of triple phase boundary (TPB) length was calculated by identifying the voxel edges in contact with elements belonging both to gas, ionic and electronic phases and summing over all particles in the structure [31].
- (iii) The specific surface area and mean phase diameter are computed from the whole reconstructed volume [31] by using mathematical morphology functions [32,33]:

- The geometrical covariogram $K(h)$ is a function that can be seen as a measure of the intersection between the phase and its image after a translation h of the medium. It allows determining the specific surface area S_p of a phase (which is defined as its surface area normalized by its volume) [32,33].
 - The covariance function $C(h)$ can be deduced from the geometric covariogram. This statistical function represents the probability that 2 points separated from a distance h belongs to the same phase. It contains information on the phase morphology, and can be used to calculate the characteristic length of the microstructure. This characteristic length can be directly associated to the mean particles diameter (assuming that the phase can be described by a packing of spherical particles).
- (iv) The mean particle diameter can be also deduced from the Phase Size Distribution (PSD). In the present work, the PSDs are calculated according to a pure geometrical approach [31] based on the Gavalda and Gelb method [34,35].
- (v) The 'apparent' tortuosity factors τ_i of the ionic, electronic and gas phases i are determined through the calculation of the effective diffusivities D_i^{eff} . As described in ref. [12], the local diffusive fluxes can be computed on the overall 3D reconstruction by solving the Laplace equation by Finite Elements Method (FEM):

In practice, each phase of the reconstructed domain is converted into an independent finite element mesh. The diffusive flows are then computed for each phase as a function of the 'intrinsic' or 'bulk' diffusivity D_i^{bulk} (in other words, the coefficient D_i^{bulk} refers either to (i) the 'intrinsic' gas diffusivity, or (ii) the bulk ionic conductivity of YSZ or (iii) the bulk electronic conductivity of Ni). Note that simulations are carried out with zero flux condition at the phase interface within the domain. An intermediate boundary condition is applied onto the two opposite faces along the studied direction of the simulated volume. One concentration is imposed upon the first face whereas the opposite one undergoes an imposed flux. The effective diffusion coefficient D_i^{eff} is then deduced from the numerical analysis by equating the macro homogeneous flux to the average value computed from the simulation. The "apparent" tortuosity factor τ_i is then given by the following relation:

$$D_i^{\text{eff}} = \varepsilon_i / \tau_i D_i^{\text{bulk}} \quad (1)$$

with ε_i the volume fraction of the considered phase. This parameter was calculated on volumes with a voxel size of 100 nm. As shown in ref. [31], this resolution is still sufficient to accurately describe the fine microstructure of typical SOEC Ni–YSZ functional layers.

4. Results and discussion

4.1. Three-dimensional reconstructions of Ni–YSZ functional layers

Data were acquired during the tomography experiments with a field of view that has allowed the reconstruction of cylindrical volume of $51.2 \times 26^2 \times \pi \mu\text{m}^3$. These raw volumes include the LSCF anode, the 8YSZ electrolyte, the Ni–8YSZ functional layer and a part of the cell support.

It can be noticed that microstructural analysis performed on LSCF anode volumes was reported elsewhere in ref. [36]: LSCF reconstructions were compared to volumes obtained from Focused Ion Beam-Scanning Electron Microscopy (FIB-SEM). Similar electrode properties were extracted from both reconstructions [36] (even if the X-ray nano-tomography yields a better statistical representation of heterogeneous electrode thanks to larger

reconstructed volumes). For example, the LSCF porosity was found to 36.6% and 36.8%, respectively for the SEM-FIB and X-ray holotomography samples. The covariance functions $C(h)$ were also very similar, meaning that morphological features are identical for both kinds of reconstructions. This comparison allows validating the accuracy and the reliability of the present Ni–YSZ reconstructions extracted for the same X-ray tomography experiment.

Besides, only a very slight evolution of LSCF morphology was found during the long term test. On the basis of this result, it is assumed hereafter that the LSCF microstructure remains stable in operation (see section 4.3).

Unlike the anode, a strong microstructural change of the cathode functional layer is observed. These microstructural evolutions are revealed in Fig. 3: the two micrographs correspond to the transverse cross sections extracted from the reconstructions before and after cell operation. The 2D slices have been taken in the middle of the functional layer and are parallel to the electrode/cathode interface. Moreover, the functional layer imaging seems also to indicate that the evolution in cermet microstructure should be mainly ascribed to an extensive Ni particle coarsening, whereas the YSZ backbone would remain unchanged after operation.

In order to verify this claim and to quantify the impact of such evolution on the electrode properties, the digitised cylindrical volumes of functional layers have been split into several non-overlapping cubic domains. These sub-volumes have been considered as Stochastic Volume Elements (SVEs) [33] and the electrode properties have calculated by averaging the values obtained on these independent realisations.

Moreover, in order to avoid any shortcoming, the sub-volumes have been selected in the middle of the functional layer, and the size of the cubic sub-volumes have been restricted to a maximum length ($\leq 8 \mu\text{m}$) which is slightly lower than the actual functional layer thickness ($\leq 10 \mu\text{m}$). Indeed, it has been shown in previous studies [36,37] that the microstructure properties of the functional layer present a gradient when approaching to the current collector substrate (in the region close to the interface between the functional layer and the cell support).

The 3D rendering sub-volumes related to the Ni–YSZ functional layers before and after cell operation are illustrated in Fig. 4a, b and c.

4.2. Ni–YSZ microstructure evolution upon SOEC operation

4.2.1. Phase volume fraction and specific surface areas

Volume fraction and specific surface area of each phase (porous phase, YSZ and Ni) are reported in Table 1.

For the reference cell, the porosity of the cathode functional layer is measured to 20% with a very low uncertainty ($\pm 0.3\%$). It can be noticed that this value of pore fraction is consistent with the rough approximation of this property measured on the 2D SEM micrographs (i.e. $\approx 18\%$: see Section 2.1). Therefore, in addition to the comparison of LSCF X-ray tomography with SEM-FIB reconstructions, the present remark on cermet porosity is a supplementary element that tends to prove the reliability of the tomographic experiment. Moreover, it is worth noting that a previous article was specifically dedicated to the validation of holotomography technique regarding the cermet reconstruction [38]: in this previous study, a direct comparison on the same region of the microstructure was conducted between X-ray tomography and SEM observations. A good matching was found between the two images that has allowed to claim the relevance and the reliability of holotomography method regarding SOEC/SOFC cermet microstructural characterisations.

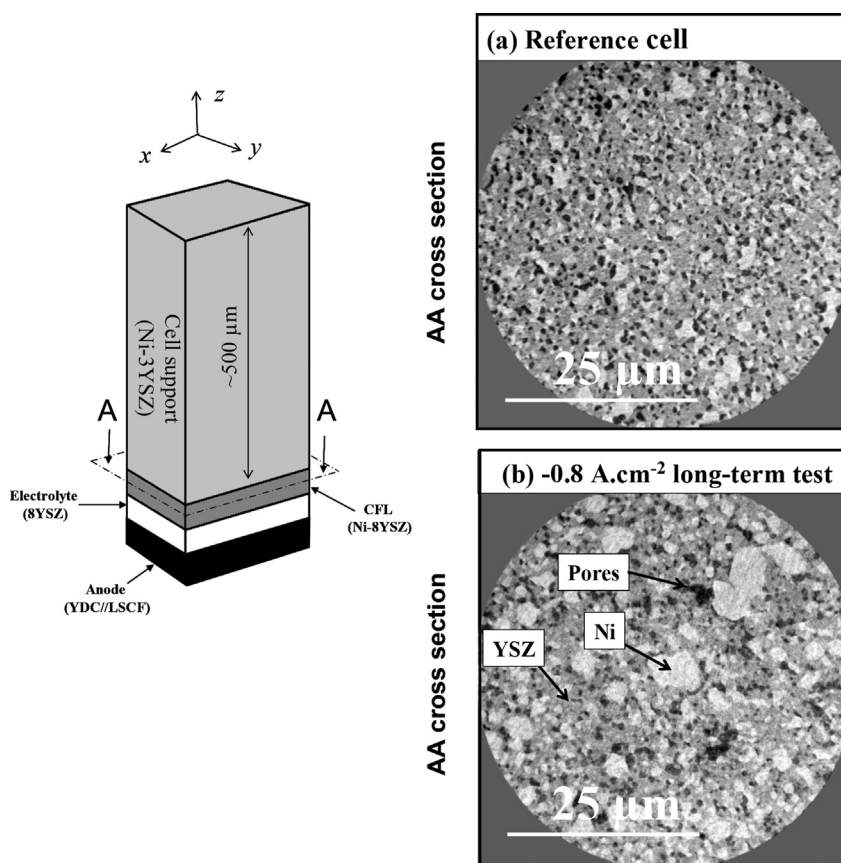


Fig. 3. Transverse cross sections extracted from the reconstructions recorded for (a) the reference cell and (b) after cell operation at $i = -0.8 \text{ A cm}^{-2}$ ($T = 800^\circ\text{C}$, 1000 h). The 2D planes have been taken in the middle of the functional layer and are parallel to the electrolyte/cathode interface.

For the YSZ phase, it can be remarked that the mean values present a scattering that remains within the uncertainties of the results. From that point of view, it can be claimed that both volume fractions and specific surface areas of YSZ phase remain identical before and after the long term test. This statement confirms that the structural morphology of the YSZ backbone is not affected by cell operation. This result is consistent with the fact that any substantial sintering of YSZ ceramic is highly unlikely at 800°C .

Nevertheless, it must be pointed out that the YSZ network of the cermet is liable to creep in operation [39]. This phenomenon is expected to occur within the functional layer that is submitted to the highest internal tensile stresses [40,41]. However, even if considering a complete internal stress relaxation, the level of plastic strain that can be reached in the layer is very low [41]. Moreover, it is worth reminding that the viscoplastic deformation of YSZ does not affect the phase volume fraction.

Unlike YSZ, it is found that the specific surface area of Ni and pores significantly decrease after the long term tests (Table 1). It can be noticed that a larger modification is found for the highest applied current density. These results are consistent with the Ni phase coarsening that must result in the decrease of Ni specific surface areas.

In addition, it is observed that the volume fraction of both pores and Ni phases is roughly stable in operation whatever the current density applied during the test. Nonetheless, from the result provided in Table 1, it seems that the functional layer could be enriched by Ni after the long test operation. Indeed, although the evolution lies in the limit of the data uncertainties, it seems that the volume fraction of Ni is slightly increased after operation. This trend could be consistent with the local morphological change of Ni reported in

SOFC mode. Indeed, a vaporisation–deposition mechanism could occur in operation and lead to a Ni redistribution in the cermet electrode [20,42,43]. Moreover, this phenomenon could be reinforced at high steam content [20,42,43] corresponding to the present testing conditions (i.e. in SOEC mode with 10% H_2 –90% H_2O). According to the proposed mechanism, vaporisation of Ni under gaseous hydroxides molecules $\text{Ni}(\text{OH})_2(\text{g})$ could be favoured where the steam partial pressure is the highest: that is to say in a region close to the cermet free surface at the cell inlet. The subsequent deposition could preferentially take place in the functional layer at the cell outlet where the reducing conditions are the highest. However, further experiments are needed to validate this assumption by mapping the Ni coarsening as a function of the position in the cermet.

4.2.2. Phase size distribution (PSD) and mean particle diameter

The characteristic lengths associated to the mean phase diameters have been determined from the covariance function (Table 2). It can be noticed that mean diameters given in Table 2 are consistent with the characteristic dimensions of the microstructure observed on the SEM image (see Fig. 2 and Section 2.1).

It is found that the mean particle diameter of nickel increases from $1.562 \pm 0.024 \mu\text{m}$ for the reference to $2.688 \pm 0.25 \mu\text{m}$ and 3.266 ± 1.732 after the -0.5 and -0.8 A cm^{-2} long-term tests, respectively. As it can be noticed in Table 2, the mean diameter for pores also increases in operation while the one related to the YSZ phase does not change. These results are directly linked to the Ni coarsening observed in Fig. 3 that results in larger metallic particles within the cermet. It can be pointed out that longer times of ageing should lead to an asymptotic value for the Ni particle size. Indeed,

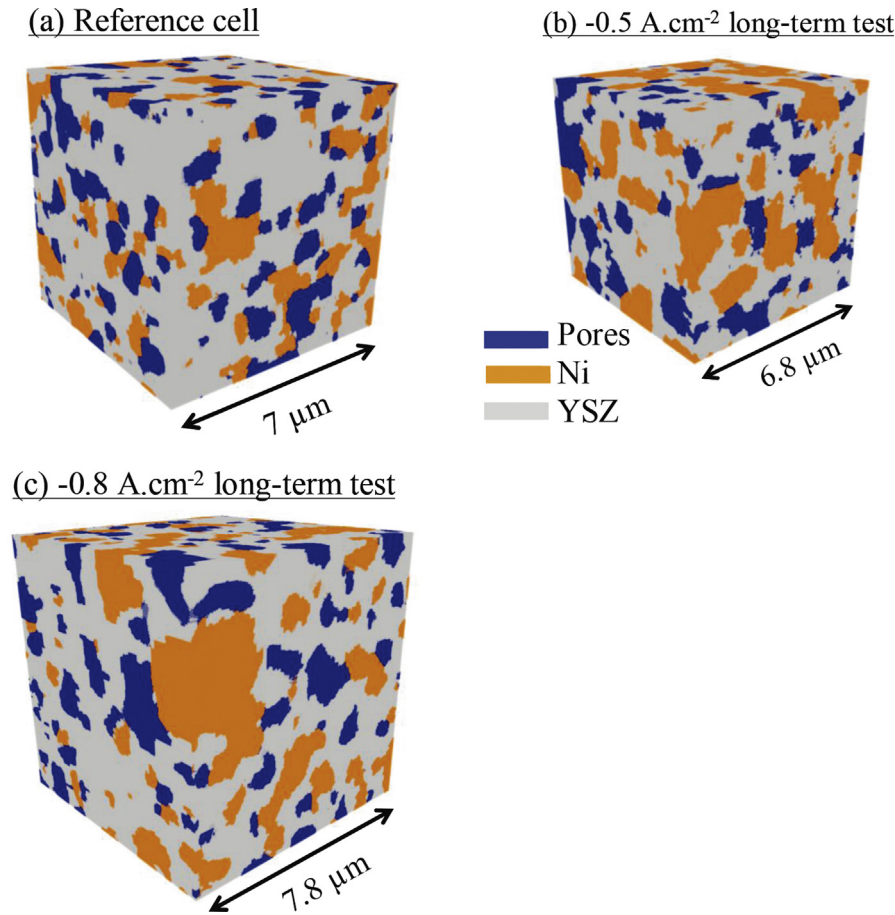


Fig. 4. 3D reconstructions of Ni–YSZ of a (a) reference, (b) –0.5 and (c) –0.8 A cm^{–2} long term tested samples. Nickel phase is orange, the porosity is blue and YSZ is grey. (For interpretation of the references to colour in this figure legend, the reader is referred to the web version of this article.)

in SOFC mode, it has been stated that Ni particles ‘displayed the biggest change in morphology during the first part of operation’ [44]. From that point of view, the measure of Ni particle diameter for different operating times should allow to calibrate a model describing the Ni agglomeration rate [44].

The Particle Size Distributions (PSDs) of Ni and YSZ are plotted in Fig. 5. First of all, it can be remarked that the PSD provides smaller mean particles diameter than the covariance function. Indeed, as already discussed in ref. [20,31], the continuous PSD leads to underestimate the real mean particle diameter.

As expected, it can be observed in Fig. 5 that the particle size distribution of Ni is shifted towards larger diameters after operation. In other words, the Ni coarsening is due to the Ni agglomeration of the smallest particles in the cermet. From that point of

view, once all the smallest Ni particles have been rearranged in biggest ones, the rate of agglomeration should slow down upon the elapsed time of operation. Note that this trend has already been observed in SOFC mode [20,44].

Finally, it can be observed that even the smallest particles of YSZ phase remains unchanged after operation. That means that the ceramic phase is stable even in the vicinity of the narrow necks between YSZ particles.

4.2.3. Triple phase boundary (TPB) lengths

It is found that the density of TPB lines decreases from 10.49 ± 1.18 μm^{–2} for the reference cell down to 7.14 ± 1.06 μm^{–2}

Table 1
Volume fractions of the three phases (–) and specific surface areas computed through the geometric covariogram method (μm^{–1}).

	Reference	–0.5 A cm ^{–2} long-term test	–0.8 A cm ^{–2} long-term test
<i>Volume fraction (–)</i>			
Porous phase	0.201 ± 0.003	0.17 ± 0.03	0.20 ± 0.04
YSZ	0.56 ± 0.03	0.51 ± 0.08	0.52 ± 0.04
Ni	0.24 ± 0.03	0.32 ± 0.06	0.28 ± 0.04
<i>Specific surface areas (μm^{–1})</i>			
Porous phase	11.37 ± 0.57	10.63 ± 1.75	8.66 ± 1.11
YSZ	6.02 ± 0.37	6.33 ± 0.40	5.66 ± 0.30
Ni	9.63 ± 0.59	7.11 ± 2.02	6.70 ± 1.08

Table 2
Mean particle diameters computed from the covariance function (μm), Tortuosity factors (–) and density of TPB lengths (μm^{–2}).

	Reference	–0.5 A cm ^{–2} long-term test	–0.8 A cm ^{–2} long-term test
<i>Mean particle diameters (μm)</i>			
Porous phase	0.900 ± 0.082	1.274 ± 0.156	2.074 ± 0.596
YSZ	1.738 ± 0.188	1.688 ± 0.488	1.982 ± 0.552
Ni	1.562 ± 0.024	2.688 ± 0.25	3.266 ± 1.732
<i>Tortuosity Factor (–)</i>			
Porous phase	9.76 ± 1.48	<i>idem</i>	<i>idem</i>
YSZ	1.62 ± 0.10	1.69 ± 0.19	1.8 ± 0.33
Ni	13.10 ± 0.58	6.31 ± 1.42	6.94 ± 1.03
<i>Density of TPB lengths (μm^{–2})</i>			
TPB	10.49 ± 1.18	7.14 ± 1.06	6.18 ± 0.6

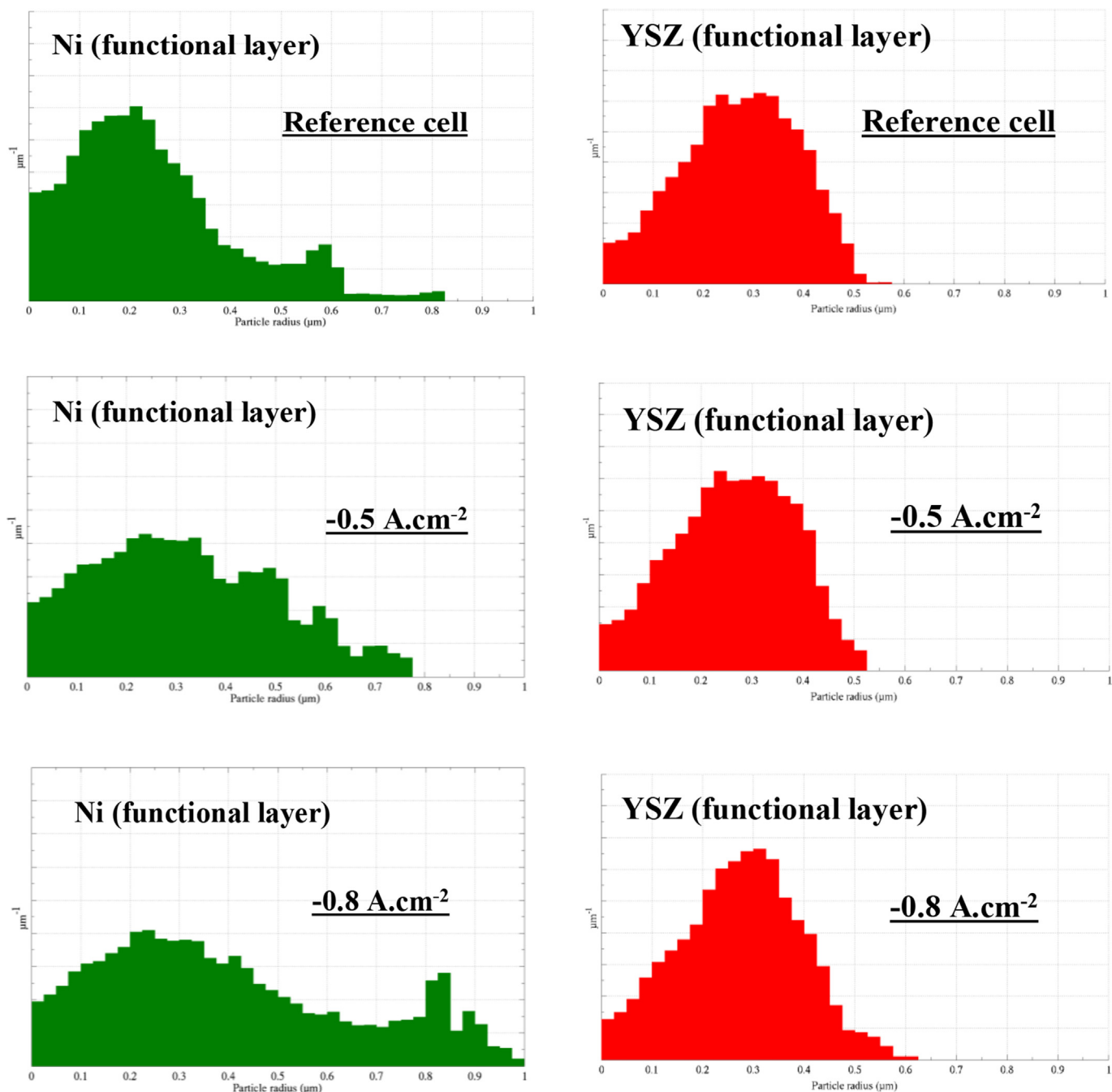


Fig. 5. Particle size distributions of Ni and YSZ. PSDs are given for the reference cell and after cell operation at $i = -0.5 \text{ A cm}^{-2}$ and $i = -0.8 \text{ A cm}^{-2}$ ($T = 800^\circ\text{C}$, 1000 h).

and $6.18 \pm 0.6 \mu\text{m}^2$ for the -0.5 A cm^{-2} and -0.8 A cm^{-2} tested samples, respectively (Table 2). Note that the initial density of TPB lengths before ageing is roughly similar to values reported in literature (9.36 and $10.58 \mu\text{m}^{-2}$ [45], or $17.9 \mu\text{m}^{-2}$ for e.g. for [16]).

The percentage decrease in density of TPB lines is 32% at $i = -0.5 \text{ A cm}^{-2}$ and 41% at $i = -0.8 \text{ A cm}^{-2}$ (for 1000 h at $T = 800^\circ\text{C}$). It can be expected that such deterioration in electrochemical active sites will significantly affect the electrode efficiency (see Section 4.3). This evolution in TPB length density is obviously caused by the Ni agglomeration during the long term test, and is consistent with the previously reported evolutions of Ni specific surface area and particle size distribution.

It can be noticed that the decrease in TPB lengths density associated to Ni particle diameter is slightly dependant on the

current density. It seems that the Ni agglomeration is promoted through the current density. This result could be explained by the atmosphere conditions in the cermet linked to the applied current density. Indeed, a higher current density should induce a more reducing atmosphere in the functional layer, which could favour the Ni re-deposition according to the mechanism previously discussed. Moreover, a higher current density could also result in a higher local temperature that directly governs the Ni sintering.

4.2.4. 'Apparent' tortuosity factors

Tortuosity factors have been calculated for the three phases (i.e. gas, nickel, YSZ) (Table 2). It is found that the tortuosity factor of the YSZ phase is equal to around 1.7 and remains stable during the tests

(from 1.62 ± 0.10 for the reference sample to 1.69 ± 0.19 and 1.80 ± 0.33 , respectively, for the -0.5 and -0.8 A cm^{-2} long-term tests: see Table 2). The average tortuosity factor of gas phase is equal to 9.76 ± 1.48 . That corresponds to a fairly high value which is directly correlated with the relative low porosity of the functional layer (i.e. $\approx 20\%$: see Table 1).

It is found that the tortuosity factor of nickel is almost divided by a factor of 2 after the long term tests. Indeed, its value decreases from 13.10 ± 0.58 for the reference sample to 6.31 ± 1.42 and 6.94 ± 1.03 , respectively, for the -0.5 and -0.8 A cm^{-2} long-term tests (Table 2). In other words, the effective Ni conductivity of the functional layer might be improved after ageing as a result of morphological evolution. This is an unexpected effect that could be explained since the mean Ni particle diameter after operation becomes large compared to the $10 \text{ }\mu\text{m}$ thickness of the functional layer (see Table 2).

4.3. Effect of microstructure changes on electrode and cell polarisations

4.3.1. Degradation of the electrode performance

The impact of microstructural evolution on electrode performance was studied through an in-house micro-model operating in SOEC mode. The model has been already detailed in a previous article [22] and summarized in Ref. [31]. The program is implemented in Matlab®. This local approach considers an isothermal slice of electrode by distinguishing the functional layer to the cell support. It takes into account the microstructure properties of ionic, electronic and gas phases (triple phase boundary, tortuosity factor,...) as well as the processes occurring therein. The model allows computing the repartition of mass, charge and reactions kinetics within the electrode structure. The electrode potential E , which corresponds to the difference in electrical potentials between electronic and ionic conducting phases, is also determined all along the electrode thickness. The “apparent” or “resulting” potential \bar{E} is defined as electronic and ionic potentials taken from each side of the functional layer [31]. The electrode polarisation curve is then expressed as the relationship between the electrode overpotential $\eta = \bar{E} - E_{i=0}$ and the current density i .

The previously determined electrode microstructure parameters have been introduced in the micro model: Fig 6 shows the evolution of the computed polarisation curves before and after ageing. For a given current density, it can be observed that the electrode overpotentials significantly increase after the long term tests. However, only a slight difference is found between the -0.5 and -0.8 A cm^{-2} long-term tests (while a significant loss in performance is stated between the reference cell and the aged ones).

In order to quantify the performance decrease, the “apparent” electrode exchange current density i_0 has been determined before and after cell operation. For this purpose, the computed electrode polarisation curves have been fitted by the expression of the activation overpotential that derives from the Butler–Volmer relation [23,31]:

$$\eta_{\text{act}} = \frac{RT}{F} \sinh^{-1} \left(\frac{i}{2i_0} \right) \quad (2)$$

where R denotes the ideal gas constant, F the Faraday constant and T the temperature. Note that the fitting is carried out over a restricted range of current density so that the partial pressures evolution across the electrode, and hence the electrode concentration overpotentials, remain negligible (i.e. $|i| \leq 0.5 \text{ A cm}^{-2}$) (Fig. 6). In these conditions, it is found that the apparent exchange current density i_0 is decreased from 537 mA cm^{-2} for the reference cell down to 417 mA cm^{-2} for the -0.8 A cm^{-2} long-term tested

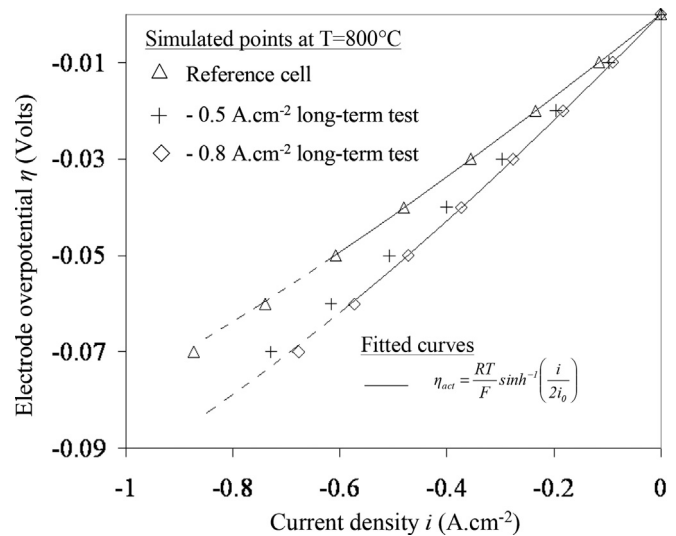


Fig. 6. Cathode polarization curves computed at $800 \text{ }^{\circ}\text{C}$ in $10\% \text{ H}_2\text{--}90\% \text{ H}_2\text{O}$. The simulated points obtained with the microstructure of the reference cell is compared to the ones determined with the electrode microstructures of the -0.5 and (c) -0.8 A cm^{-2} long term tested samples. The fitted curves to obtain the ‘apparent’ exchange current densities of electrode are also shown.

electrode. That corresponds to a deterioration rate of 22.3% per 1000 h only caused by the Ni agglomeration.

In order to grasp the effect of each parameter evolution on the result, a sensitivity analysis has been performed by changing the microstructural properties one by one, the others remaining in the reference case. It has been stated that the decrease in the electrode performance is mainly related to the loss of TPB length density, since it represents more than 90% of the current density loss. For example, 92% of the current density reduction for an overpotential $\eta = -0.2 \text{ V}$ is caused by a decrease in the TPB length from $10.49 \pm 1.18 \text{ }\mu\text{m}^{-2}$ to $7.14 \pm 1.06 \text{ }\mu\text{m}^{-2}$ (which corresponds to the TPB length density obtained on the -0.5 A cm^{-2} tested sample). Accordingly, within the range of microstructural evolution previously reported, it has been found that the modifications of tortuosity factors of both gas and electronic conducting (Ni) phases do not significantly affect the electrode response. Indeed, as already stated in Ref. [22], the effective gas diffusion and electronic transfer through the thin functional layer do not govern the electrode behaviour since these processes are not limiting.

4.3.2. Degradation of the cell performance

In order to estimate the impact of Ni agglomeration on global cell performance, the cathode exchange current densities determined before and after cell operation were used as an input data in an in-house “macroscopic” model. At this scale, the model describes as well as the geometry of the complete cell than the interconnect plates that ensure the current collection and the gas distribution along the cell. The model encompasses a combined electrochemical, thermal and mass transfer description of the electrolyser. The governing equations of this numerical tool are presented in details in reference [23] whereas an experimental validation can be found in reference [46]. This numerical tool has been used in the present work in isothermal condition considering a planar geometry with a radial co-flow configuration. These conditions are representative for the test bench used for the cell testings [25,46]. Table 3 gathers the operating conditions and material data used the simulations.

As shown in Fig. 7a, the cell performance calculated for the ‘fresh’ cell matches the experimental polarisation curves (as already stated in ref. [46]).

Table 3
Conditions of simulations at the cell level.

Temperature	$T = 800\text{ }^{\circ}\text{C}$
Gas flow configuration	Radial co-flow configuration representative for the test bench [25,46]
Inlet gas composition	Cathode: 10% H_2 –90% H_2O — Anode: Air
Inlet gas flux	Cathode: $12\text{ Nml min}^{-1}\text{ cm}^{-2}$ — Anode: $12\text{ Nml min}^{-1}\text{ cm}^{-2}$
'Apparent' electrode exchange current densities	Anode: 200 mA cm^{-2} [23,46], Cathode: 537 mA cm^{-2} for the reference cell and 417 mA cm^{-2} for the -0.8 A cm^{-2} long-term test (see Fig. 6 and Section 4.3)
Contact resistances	$R_c = 0.07\text{ }\Omega\text{ cm}^2$ (determined by Impedance spectroscopy [25]).
Microstructure properties of the cell support	Porosity: 0.326 ^a , Mean pore radius: $1\text{ }\mu\text{m}^a$ Tortuosity factor: 7 ^b .

^a Estimated by image analysis on a polished cross section observed with a scanning electron microscope (in back-scattering electrons mode).

^b Adjusted on the experimental polarisation curves.

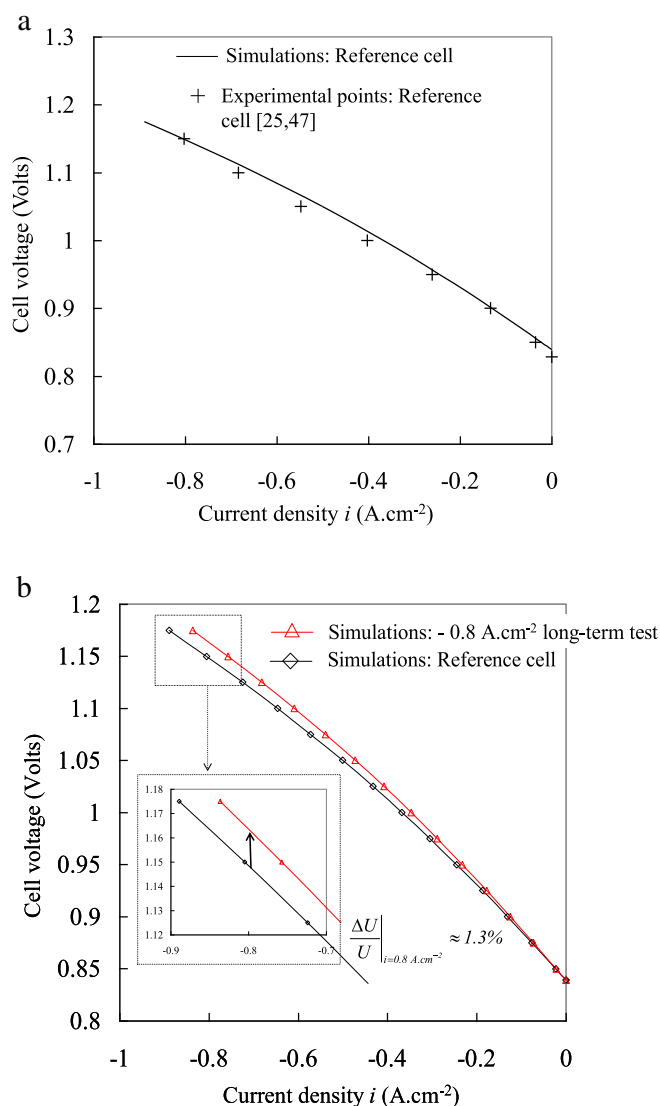


Fig. 7. Cell polarisation curves at $T = 800\text{ }^{\circ}\text{C}$ (see Table 3 for all the conditions of simulations). a: Comparison between the simulated curve and the experimental data for the reference cell. b: Simulated curves before and after cell operation at $i = -0.8\text{ A cm}^{-2}$ for 1000 h [47].

Fig. 7b illustrates the SOEC polarisation curves computed for the reference case and after the cell operation at $i = -0.8\text{ A cm}^{-2}$ for 1000 h. The insert shows a zoom on the U – i curves: at an operating current density of -0.8 A cm^{-2} , the computed voltage increase is equal to $\Delta U/U \approx 1.3\%$. In other words, the microstructural parameters evolution characterized in this work after a -0.8 A cm^{-2} long term test leads to a cell degradation rate of 1.3% per 1000 h, whereas the actual voltage deterioration, that has been experimentally recorded, was about 10% per 1000 h [25]. As a consequence, in our conditions, the Ni coarsening quantified by 3D analysis can only explain a part of the global cell electrochemical degradation. From this point of view, some other causes of progressive electrode degradation need to be explored.

In this frame, the anode LSCF destabilisation and/or delamination could also significantly contribute to the global cell performance loss. In our cases, SEM observations of LSCF//YDC//YSZ interfaces after testing have not revealed any interfacial debonding. Synchrotron X-ray Absorption Spectroscopy (XAS) was also performed on the anodes. The characterization has highlighted an LSCF chemical decomposition that could significantly contribute to the overall cell voltage loss. The results of this characterization have been already detailed and published in reference [36]. Among the other causes of degradation, the YSZ phase crystallographic transformation in the cathode functional layer could also contribute to the overall cell voltage loss [22]. It is expected that all these phenomena might have a strong impact on the electrode performance. From that discussion, it can be claimed that the global electrochemical degradation cannot be explained only by one phenomenon, but is the result of different causes. All these causes stem from an insufficient cell materials and microstructure stability at high temperature. Nevertheless, it can be pointed out that the continuation of Ni coarsening over long term operation ($>1000\text{ h}$) may cause the loss of metallic particle connectivity and would result in a sharp loss in cell performance when the percolation threshold is reached.

5. Conclusions

Microstructural evolution of a Solid Oxide Electrolyser Cell (SOEC) Ni–YSZ cathode was investigated using synchrotron X-ray nano-holotomography technique. Electrode 3D reconstructions have been obtained on a reference cell and on long-term tested cells (for two distinct current densities: 1000 h at $800\text{ }^{\circ}\text{C}$ at -0.5 and -0.8 A cm^{-2}).

Microstructural properties extracted from the 3D reconstructions, such as the tortuosity factor and the triple phase boundary length density, exhibit a remarkable evolution during the long term tests. Evolutions of morphological parameters were introduced in in-house micro and macro models to evaluate their impacts on the electrode and cell degradation. It has been found that the decrease in density of TPB length yield a cathode degradation rate of $\approx 22\%/1000\text{ h}$ (at $T = 800\text{ }^{\circ}\text{C}$, $i = -0.8\text{ A cm}^{-2}$ and 10% H_2 –90% H_2O). This loss in electrode performances results in a cell voltage increase of 1.3%/1000 h that explains only a part of the experimentally measured degradation rates.

Acknowledgements

This work has been achieved in the framework of ANDES research programme, funded by the CEA.

The authors would like to thank J.-M. Fabbri for the sample preparation on the CEA Nano-Characterization Platform (PFNC).

References

- [1] J. Schefold, A. Brisse, F. Tietz, J. Electrochem. Soc. 159 (2012) A137–A144.
- [2] A. Hauch, S.D. Ebbesen, S.H. Jensen, M. Mogensen, J. Electrochem. Soc. 155 (2008) B1184–B1193.
- [3] G. Schiller, A. Ansar, M. Lang, O. Patz, J. Appl. Electrochem. 39 (2009) 293–301.
- [4] M.A. Laguna-Bercero, R. Campana, A. Larrea, J.A. Kilner, V.M. Orera, J. Power Sources 196 (2011) 8942–8947.
- [5] A.V. Virkar, Int. J. Hydrogen Energy 35 (2010) 9527–9543.
- [6] J.R. Mawdsley, J.D. Carter, A.J. Kropf, B. Yildiz, V.A. Maroni, Int. J. Hydrogen Energy 34 (2009) 4198–4207.
- [7] R. Knibbe, M.L. Traulsen, A. Hauch, S.D. Ebbesen, M. Mogensen, J. Electrochem. Soc. 157 (2010) B1209–B1217.
- [8] C. Bernuy-Lopez, R. Knibbe, Z. He, X. Mao, A. Hauch, K.A. Nielsen, J. Power Sources 196 (2011) 4396–4403.
- [9] A. Hauch, J.R. Bowen, L.T. Kuhn, M. Mogensen, Electrochem. Solid-state Lett. 11 (3) (2008) B38–B41.
- [10] M.A. Laguna-Bercero, R. Campana, A. Larrea, J.A. Kilner, V.M. Orera, J. Electrochem. Soc. 6 (2010) B852–B855.
- [11] J. Schefold, A. Brisse, M. Zahid, J. Electrochem. Soc. 159 (2009) B897–B904.
- [12] J. Laurencin, R. Quey, G. Delette, H. Suhonen, P. Cloetens, P. Bleuet, J. Power Sources 198 (2012) 182–189.
- [13] N. Vivet, S. Chupin, E. Estrade, T. Piquero, P.L. Pommier, D. Rochais, E. Bruneton, J. Power Sources 196 (2011) 7541–7549.
- [14] J.R. Wilson, J. Scott Cronin, Scott A. Barnett, Scr. Mater. 65 (2011) 67–72.
- [15] G.J. Nelson, Kyle N. Grew, John R. Izzo Jr., Jeffrey J. Lombardo, William M. Harris, Antonin Faes, Aïcha Hessler-Wyser, Jan Van Herle, Steve Wang, Yong S. Chu, Anil V. Virkar, Wilson K.S. Chiu, Acta Mater. 60 (2012) 3491–3500.
- [16] P.R. Shearing, J. Gelb, J. Yi, W.-K. Lee, M. Drakopoulos, N.P. Brandon, Electrochem. Commun. 12 (2010) 1021–1024.
- [17] D. Kanno, N. Shikazono, N. Takagi, K. Matsuzaki, N. Kasagi, Electrochim. Acta 56 (2011) 4015–4021.
- [18] H. Iwai, N. Shikazono, T. Matsui, H. Teshima, M. Kishimoto, R. Kishida, D. Hayashi, K. Matsuzaki, D. Kanno, M. Saito, H. Muroyama, K. Eguchi, N. Kasagi, H. Yoshida, J. Power Sources 195 (2010) 955–961.
- [19] M. Kishimoto, H. Iwai, M. Saito, H. Yoshida, J. Power Sources 196 (2011) 4555–4563.
- [20] L. Holzer, B. Iwanschitz, Th. Hocker, B. Münch, M. Prestat, D. Wiedenmann, U. Vogt, P. Holtappels, J. Sfeir, A. Mai, Th. Graule, J. Power Sources 196 (2011) 1279–1294.
- [21] Z. Jiao, N. Shikazono, N. Kasagi, J. Electrochem. Soc. 159 (2012) B285–B291.
- [22] E. Lay-Grindler, J. Laurencin, G. Delette, J. Aicart, M. Petitjean, L. Dessemond, Int. J. Hydrogen Energy 38 (2013) 6917–6929.
- [23] J. Laurencin, D. Kane, G. Delette, J. Deseure, F. Lefebvre-Joud, J. Power Sources 196 (2011) 2080–2093.
- [24] T. Ishihara, N.M. Sammes, O. Yamamoto, Chapter 4: electrolytes, in: Subhash C. Singhal, K. Kendall (Eds.), High temperature solid oxide fuel cells, fundamentals, design and applications, Elsevier, 2003, p. 91.
- [25] A. Mansuy, Ph.D. Grenoble, France, 2012.
- [26] J. Villanova, J. Laurencin, P. Cloetens, P. Bleuet, G. Delette, H. Suhonen, F. Usseglio-Viretta, J. Power Sources 243 (2013) 841–849.
- [27] P. Perona, J. Malik, IEEE Trans. Pattern Anal. Mach. Intel. 12 (1990) 629–639.
- [28] N. Otsu, IEEE Trans. Syst. Man. Cybern. SMC 9 (1979) 62–66.
- [29] J. Joos, T. Carraro, A. Weber, E. Ivers-Tiffée, J. Power Sources 196 (2011) 7302–7307.
- [30] <http://www-cast3m.cea.fr>
- [31] F. Usseglio-Viretta, J. Laurencin, G. Delette, J. Villanova, P. Cloetens, D. Leguillon, J. Power Sources 256 (2014) 394–403.
- [32] A. Haas, G. Matheron, J. Serra, Ann. Des. Mines (1967) 39–57.
- [33] T. Kanit, S. Forest, I. Galliet, V. Mounoury, D. Jeulin, Int. J. Solids Struct. 40 (2003) 3647–3679.
- [34] L.D. Gelb, K.E. Gubbins, Langmuir 15 (1999) 305–308.
- [35] V. Morales-Florez, M. Pinero, N. de la Rosa-Fox, L. Esquivias, J.A. Anta, J. Primera, J. Non-cryst. Solids 354 (2008) 193–198.
- [36] E. Lay-Grindler, J. Laurencin, J. Villanova, I. Kieffer, F. Usseglio-Viretta, T. Le Bihan, P. Bleuet, A. Mansuy, G. Delette, ECS Trans. 57 (1) (2013) 3177–3187.
- [37] J. Joos, M. Ender, I. Rotscholl, N.H. Menzler, E. Ivers-Tiffée, J. Power Sources 246 (2014) 819–830.
- [38] R. Quey, H. Suhonen, J. Laurencin, P. Cloetens, P. Bleuet, Mater. Charact. 78 (2013) 87–95.
- [39] J. Laurencin, G. Delette, F. Usseglio-Viretta, S. Di Iorio, J. Euro. Ceram. Soc. 31 (2011) 1741–1752.
- [40] J. Laurencin, G. Delette, F. Lefebvre-Joud, M. Dupeux, J. Euro. Ceram. Soc. 28 (2008) 1857–1869.
- [41] J. Laurencin, V. Roche, C. Jaboutian, I. Kieffer, J. Mougín, M.C. Steil, Int. J. Hydrogen Energy 37 (2012) 12557–12573.
- [42] Z. Jiao, N. Takagi, N. Shikazono, N. Kasagi, J. Power Sources 196 (2011) 1019–1029.
- [43] J. Sehested, Catal. Today 111 (2006) 103–110.
- [44] P. Tanasini, M. Cannarozzo, P. Costamagna, A. Faes, J. Van Herle, A. Hessler-Wyser, C. Cominellis, Fuel Cells 9 (5) (2009) 740–752.
- [45] P.R. Shearing, J. Golbert, R.J. Chater, N.P. Brandon, Chem. Eng. Sci. 64 (2009) 3928–3933.
- [46] J. Aicart, J. Laurencin, M. Petitjean, L. Dessemond, Fuel Cells 14(3) (2014) 430–477.
- [47] J. Mougín, A. Mansuy, A. Chatroux, G. Gousseau, M. Petitjean, M. Reytyer, F. Mauvy, Fuel Cells 13 (4) (2013) 623–630.